

VLA FRAMEx. II. Radio Spectra of Nearby Active Galactic Nuclei at Subarcsecond Resolution

ANDREW J. SARGENT ^{1,2} ALEXANDER J. VAN DER HORST ² MEGAN C. JOHNSON ³ TRAVIS C. FISCHER ⁴
NATHAN J. SECREST ¹ PHIL J. CIGAN ¹ ONIC I. SHUVO ⁵ AND KRISTA L. SMITH ⁶

¹United States Naval Observatory, 3450 Massachusetts Ave., NW, Washington, DC 20392, USA

²Department of Physics, The George Washington University, 725 21st St. NW, Washington, DC 20052, USA

³National Science Foundation, 2415 Eisenhower Ave., Alexandria, VA 22314, USA

⁴AURA for ESA, Space Telescope Science Institute, 3700 San Martin Drive, Baltimore, MD 21218, USA

⁵Department of Physics, University of Maryland Baltimore County, 1000 Hilltop Circle, Baltimore, MD 21250, USA

⁶Department of Physics and Astronomy, Texas A&M University, 578 University Drive, College Station, TX 77843, USA

ABSTRACT

We present 4 – 12 GHz in-band spectral energy distributions with accompanying 6 GHz and 10 GHz imaging results for a volume-complete sample (< 40 Mpc) of hard X-ray selected active galactic nuclei (AGNs) observed with the Karl G. Jansky Very Large Array (VLA) in its A-array configuration. Despite expectations, only 12 out of 25 of these targets have been detected by the Very Long Baseline Array (VLBA) at milliarcsecond resolution in our previous studies, and we aim to understand the nature of why the circumnuclear radio emission resolves away at the subparsec spatial scales. We find that the sources not detected by the VLBA are also the faintest sources observed with the VLA. We explore the spectral structure derived from the nuclear emission and measure a mean spectral index of $\langle \alpha \rangle = -0.69$ with a scatter of $\sigma_\alpha = 0.18$ for the sources not detected by the VLBA, indicative of optically thin synchrotron emission. The 12 sources detected by the VLBA primarily have flat ($-0.5 \leq \alpha \leq 0.0$) or inverted ($\alpha > 0$) spectral indices. Nine of the sources have statistically significant curvature, with only one that was not detected by the VLBA. In NGC 3079, we model an approximately flat spectrum for the excess emission observed by the VLA that is likely produced entirely beyond parsec spatial scales.

1. INTRODUCTION

Dynamical evidence has shown that supermassive black holes (SMBHs, with masses $> 10^6 M_\odot$) with deep gravitational potentials reside at the centers of massive galaxies (Kormendy & Richstone 1995). When matter falls onto SMBHs in the form of an accretion disk, radiation is emitted across the electromagnetic spectrum and the host galaxy nuclei become active (Lynden-Bell 1969). The accretion process regulates the surrounding interstellar medium (ISM) in these active galactic nuclei (AGNs) through physical and radiative mechanisms strongly correlated with radio luminosity at GHz frequencies (de Bruyn & Wilson 1978; Fabian 2012; Panessa et al. 2019). Over time, nearby gas and dust is cleared, depriving the SMBH of necessary fuel and terminating any further AGN activity.

Measurement of the radio continuum is essential when characterizing nuclear properties of AGNs, most importantly because it is not susceptible to the effects of dust obscuration that are prominent at higher frequencies (Ho & Ulvestad 2001). An important diagnostic is the shape of the spectral energy distribution (SED), as a variety of physical mechanisms produce the radio spectral index α (defined as $S \propto \nu^\alpha$), which is typically classified as steep ($\alpha < -0.5$), flat ($-0.5 \leq \alpha \leq 0$), or inverted ($\alpha > 0$). Flat or inverted spectra may be due to attenuation from optically thick sources observed near the nucleus. For example, distributions of electrons with overlapping synchrotron spectra at radii near the base of a highly collimated relativistic jet may produce flat to inverted spectra observed along the line of sight ($-0.5 < \alpha < 2.5$, Blandford & Königl 1979). Electrons accelerated in a highly magnetized corona can also contribute to forming flat spectra through non-uniform superpositions of many synchrotron sources which are self-absorbed (de Bruyn 1976; Laor & Behar 2008). Steep spectrum sources on the other hand are observed in opti-

Table 1. VLA FRAMEx Sample

	Target	R.A. (ICRS)	Decl. (ICRS)
1	NGC 1052	02 ^h 41 ^m 04.790 ^s	−08°15′20.70″
2	NGC 1068	02 ^h 42 ^m 40.770 ^s	−00°00′47.80″
3	NGC 1320	03 ^h 24 ^m 48.690 ^s	−03°02′32.10″
4	NGC 2110	05 ^h 52 ^m 11.370 ^s	−07°27′22.40″
5	NGC 2782	09 ^h 14 ^m 05.110 ^s	+40°06′49.60″
6	IC 2461	09 ^h 19 ^m 58.030 ^s	+37°11′27.70″
7	NGC 2992	09 ^h 45 ^m 42.040 ^s	−14°19′34.80″
8	NGC 3081	09 ^h 59 ^m 29.540 ^s	−22°49′34.70″
9	NGC 3089	09 ^h 59 ^m 36.680 ^s	−28°19′52.70″
10	NGC 3079	10 ^h 01 ^m 57.800 ^s	+55°40′47.20″
11	NGC 3227	10 ^h 23 ^m 30.570 ^s	+19°51′54.20″
12	NGC 3786	11 ^h 39 ^m 42.510 ^s	+31°54′33.90″
13	NGC 4151	12 ^h 10 ^m 32.570 ^s	+39°24′21.00″
14	NGC 4180	12 ^h 13 ^m 03.050 ^s	+07°02′19.60″
15	NGC 4235	12 ^h 17 ^m 09.880 ^s	+07°11′29.60″
16	NGC 4388	12 ^h 25 ^m 46.810 ^s	+12°39′43.40″
17	NGC 4593	12 ^h 39 ^m 39.440 ^s	−05°20′39.00″
18	NGC 5290	13 ^h 45 ^m 19.160 ^s	+41°42′44.40″
19	NGC 5506	14 ^h 13 ^m 14.900 ^s	−03°12′27.20″
20	NGC 5899	15 ^h 15 ^m 03.250 ^s	+42°02′59.40″
21	NGC 6814	19 ^h 42 ^m 40.580 ^s	−10°19′25.10″
22	NGC 7314	22 ^h 35 ^m 46.190 ^s	−26°03′01.50″
23	NGC 7378	22 ^h 47 ^m 47.690 ^s	−11°48′59.80″
24	NGC 7465	23 ^h 02 ^m 00.950 ^s	+15°57′53.50″
25	NGC 7479	23 ^h 04 ^m 56.660 ^s	+12°19′22.30″

NOTE—The VLA FRAMEx sample and their ICRS coordinates used for pointing in observations.

cally thin emission regions. This emission may originate from AGN winds shocking the ISM (Zakamska & Greene 2014), old electron populations ($\gtrsim 10^7$ yr) within remnants of supernovae events (Condon 1992), or relativistic electrons accelerating along magnetized plasma in a collimated jet (Begelman et al. 1984). The radio spectrum is also often accompanied by free-free radiation, with optically thick nuclear sources potentially producing an inverted spectrum (Baskin & Laor 2021; Laor et al. 2019; Levinson et al. 1995), or the optically thin flat-spectrum H II regions associated with star formation (Condon 1992).

Measuring and interpreting the radio spectral index can be challenging. Sampling from heterogeneous surveys can complicate the determination of radio spectra, where flux density measurements may suffer from unmatched resolutions, differing (u , v)-coverage, and non-simultaneity, all of which can potentially skew the spectral index measurement (see for instance Figure 11 in Gim et al. 2019). Further restrictions apply when sensitivity preferences need to be reduced due to telescope

observing time, data volume, or computational limitations. Lastly and depending on the science goals, sample selection biases, including wavelength-dependent selection effects and incomplete galaxy samples, can complicate the statistical interpretation of spectral indices.

Nearby AGNs have frequently been observed with the Very Large Array (VLA), a 27-dish radio interferometer constructed in the 1970s, which has been used to determine their spectral properties (e.g. Rush et al. 1996; Ho & Ulvestad 2001). But a complicating issue common in the decades-old archival observations is sparse spectral coverage, often with only a few narrow-band measurements that span large frequency ranges due to the receiver limitations at the time. However, in 2012 the VLA was upgraded to the Karl G. Jansky VLA (hereafter VLA), mitigating several of the limitations. The upgrade expanded sensitivity by at least an order of magnitude from several perspectives including the continuum sensitivity ($\times 10$), bandwidth ($\times 80$), and fine frequency resolution ($\times 3180$). Additionally, the frequency coverage is now complete from 1 – 50 GHz, and allows for simultaneous sampling across 4 GHz with all polarization correlations. Therefore, the VLA offers unique advantages for constructing AGN SEDs across large frequency ranges while maintaining consistent spatial scales due to the flexibility provided by four primary antenna configurations. This was recently exemplified in Panessa et al. (2022), a multifrequency study using multiple VLA configurations to form matched resolution SEDs across 5 – 45 GHz from a sample of hard X-ray selected AGNs.

The Fundamental Reference AGN Monitoring Experiment project (FRAMEx; Dorland et al. 2020) is an observing program studying the nuclear phenomena of a hard X-ray selected volume-complete sample of 25 AGNs in the time domain. The FRAMEx sample was chosen in part to study the implied relation between the radio and X-ray luminosities observed in the fundamental plane of black hole activity (FP), that, when combined with the black hole mass, defines a paradigm unifying the ostensible core emission processes for black holes of all masses (Merloni et al. 2003; Falcke et al. 2004). We obtained high-resolution (\sim mas) Very Long Baseline Array (VLBA) snapshot observations together with *Neil Gehrels Swift Observatory* (*Swift*) X-ray Telescope (XRT) observations in Fischer et al. (2021, hereafter FRAMEx I) and used the FP to derive an expected radio luminosity with a 5σ detection threshold. Despite a 100% detection rate of the previously available archival VLA observations of the FRAMEx targets from

the NRAO VLA Archive Survey¹ (depicted in Figure 3 in [FRAMEX I](#)), detected only 9 out of 25 targets with the VLBA, an unexpected result that implies an inconsistency with the expectations of the FP relation. A reobservation campaign subsequently occurred and focused on 9 of the 16 objects that were not originally detected with the VLBA, but with four times the integration time in order to double the sensitivity as compared to the original observation ([Shuvo et al. 2022](#), hereafter [FRAMEX III](#)). Still, only 3 of the 9 targets were detected with these deeper observations, bringing the total number of FRAMEX detections to 12 out of 25. Two additional VLBA campaigns followed the snapshot observations in [FRAMEX I](#) which focused on the VLBA-detected targets. One was a monitoring campaign studying the parsec-scale variability (i.e. the original intent of FRAMEX) in the targets NGC 2992 ([Fernandez et al. 2022](#), named [FRAMEX II](#)) and NGC 3079 ([Fernandez et al. 2023](#), hereafter [FRAMEX IV](#)). [Shuvo et al. \(2024, hereafter FRAMEX V\)](#) conducted multifrequency observations of all of the VLBA-detected objects at 1.6, 4.4, 8.6, and 22 GHz to more robustly determine the true central origin of radio emission.

The discrepancy with the FP suggests that much of the radio emission observed to be coincident with the nucleus in the archival VLA data is contaminated with extranuclear radio emission that is produced beyond the resolving capabilities of the VLBA. For reference, a 6 GHz VLA observation in its most extended A-array configuration has a maximum baseline length of 36 km which sets a resolution of $\sim 0.3''$. Likewise, the smallest baseline length of 0.68 km of the VLA can resolve emission out to a largest angular scale of $\sim 9''$. Thus, at a luminosity distance of 40 Mpc the VLA can resolve emission that spans projected physical sizes of $\sim 58 - 1745$ pc. Compare this to the corresponding resolving capabilities of the VLBA set by its shortest (Pie Town–Los Alamos, 236 km) and longest baselines (Mauna Kea–St. Croix, separated by 8611 km²), which probe angular scales of $\sim 0.001'' - 0.004''$, corresponding to regions extending $\sim 0.38 - 10$ pc in physical sizes. The VLBA is therefore most sensitive to compact point sources and does not have the ability to resolve extended emission very well beyond the largest angular scale constrained by the shortest baseline. The VLBA sensitivity is further exacerbated by its sparse 10-antenna array, which provides for 45 baselines, and our one-hour snapshot observations in [FRAMEX I](#) probed to an observa-

tion sensitivity depth of $\sim 20 \mu\text{Jy bm}^{-1}$ with the full array. On the other hand, a theoretical one-hour observation with all 27 antennas (351 baselines) of the VLA achieves a sensitivity depth of $\sim 7 \mu\text{Jy bm}^{-1}$.

Therefore, this paper investigates the Stokes I radio continuum emission as a follow-up survey to [FRAMEX I](#) with new VLA observations. The observations consist of a uniform data set of the FRAMEX sample observed with the VLA in its most extended A-array configuration, resulting in the highest spatial resolution achievable with the VLA. It is also follow-up to [Sargent et al. \(2024, hereafter Paper I\)](#), where we focused on the methodology of calibration and imaging for these data, and conducted an in-depth analysis of one of the 25 sources in our sample, NGC 4388. Here we conduct an analysis of the 4 – 12 GHz spectral properties of the AGNs with a 128 MHz spectral resolution. In Section 2, we discuss the sample, calibration, and imaging procedures used for these new VLA observations. In Sections 3 and 4 we present and discuss our results, and in Section 5 we summarize our findings.

Throughout this paper we define the spectral index α as $S \propto \nu^\alpha$ and spectral curvature β as $S \propto \nu^{(\alpha+\beta \log \nu)}$, with S the flux density and ν the frequency.

2. METHODOLOGY

2.1. Sample Selection

The sample in this paper is the same as in [FRAMEX I](#), which were hard X-ray selected AGNs from the 105-month (*Swift*) Burst Alert Telescope (BAT) catalog ([Oh et al. 2018](#)). The catalog’s uniform flux limit of $\sim 8 \times 10^{-12} \text{ erg s}^{-1} \text{ cm}^{-2}$ enables a selection of all AGNs above a defined luminosity threshold out to a corresponding volume-complete luminosity distance. Thus the FRAMEX targets were selected with a hard X-ray luminosity $> 10^{42} \text{ erg s}^{-1}$, limiting the distance of the sample to all AGNs within 40 Mpc. The original FRAMEX sample selection imposed declination limits of $-30^\circ < \delta < +60^\circ$ for observational reasons, yielding 25 objects which form the basis of the present study. Table 1 lists the sample with their ICRS positions.

2.2. VLA Observations and Data Reduction

We conducted VLA observations of our 25 targets between 2020 December 10 and 2021 March 4 under the project code 20B-241 (P.I. Fischer). Most of the observations were carried out when the VLA was in the A-array configuration, but some when the VLA was transitioning to its D-array configuration after 2021 March 1 (11 out of 50 observations were affected by this tran-

¹ <http://archive.nrao.edu/nvas>

² <https://science.nrao.edu/facilities/vlba/docs/manuals/oss/ang-res>

Table 2. VLA FRAMEx Observations

Target	Band	Obs. Date	Conf.	SB ID	Primary	Interpolated	Model	Phase	
(1)	(2)	(3)	(4)	(5)	Cal.	Flux	Diff.	Cal.	
(1)	(2)	(3)	(4)	(5)	(6)	(7)	(8)	(9)	
1	NGC 1052	C	2021-01-24	A	38952694	3C 138	3.517 Jy	3.7%	J0239–0234
		X	2021-01-16	A	38953167	3C 138	2.484 Jy	6.5%	J0239–0234
2	NGC 1068	C	2021-01-26	A	39008458	3C 138	3.518 Jy	3.7%	J0239–0234
		X	2021-01-20	A	39008718	3C 138	2.485 Jy	6.6%	J0239–0234
3	NGC 1320	C	2021-01-24	A	39011072	3C 138	3.517 Jy	3.7%	J0339–0146
		X	2021-01-17	A	39175511	3C 138	2.484 Jy	6.6%	J0339–0146
4	NGC 2110	C	2021-02-04	A	39176337	3C 138	3.518 Jy	3.7%	J0541–0541
		X	2021-01-27	A	39176455	3C 138	2.488 Jy	6.7%	J0541–0541
5	NGC 2782	C	2020-12-31	A	38677768	3C 138	3.515 Jy	3.6%	J0927+3902
		X	2020-12-14	A	38952497	3C 286	J0927+3902
6	IC 2461	C	2021-02-03	A	39176799	3C 286	J0927+3902
		X	2021-01-18	A	39176643	3C 286	J0927+3902
7	NGC 2992	C	2021-02-19	A	39236874	3C 286	J0943–0819
		X	2021-01-29	A	39237182	3C 286	J0943–0819
8	NGC 3081	C	2021-01-06	A	38947401	3C 138	3.516 Jy	3.6%	J0927–2034
		X	2021-01-03	A	38954868	3C 138	2.479 Jy	6.3%	J0927–2034
9	NGC 3089	C	2021-01-12	A	38947689	3C 138	3.516 Jy	3.6%	J1037–2934
		X	2021-01-04	A	39007522	3C 138	2.479 Jy	6.4%	J1037–2934
10	NGC 3079	C	2021-02-25	A	39342314	3C 138	3.520 Jy	3.7%	J1035+5628
		X	2021-02-24	A	39342185	3C 138	2.498 Jy	7.2%	J1035+5628
11	NGC 3227	C	2021-03-02	A→D	39343798	3C 138	3.521 Jy	3.8%	J1016+2037
		X	2021-03-01	A	39343665	3C 138	2.500 Jy	7.2%	J1016+2037
12	NGC 3786	X	2021-03-03	A→D	39380922	3C 286	J1147+3501
13	NGC 4151	C	2021-02-18	A	39236054	3C 286	J1209+4119
		X	2021-01-22	A	39236360	3C 286	J1209+4119
14	NGC 4180	C	2020-12-31	A	39007910	3C 286	J1224+0330
		X	2020-12-10	A	39008114	3C 286	J1224+0330
15	NGC 4235	C	2021-03-03	A→D	39328466	3C 286	J1239+0730
		X	2021-03-01	A	39336923	3C 286	J1239+0730
16	NGC 4388	C	2021-03-03	A→D	39381834	3C 286	J1254+1141
		X	2021-03-02	A→D	39382198	3C 286	J1254+1141
17	NGC 4593	C	2021-01-01	A	38953664	3C 286	J1246–0730
		X	2020-12-18	A	38954482	3C 286	J1246–0730
18	NGC 5290	C	2021-03-01	A	39375363	3C 286	J1327+4326
		X	2021-02-28	A	39367450	3C 286	J1327+4326
19	NGC 5506	C	2021-03-02	A→D	39365069	3C 286	J1354–0206
		X	2021-03-01	A	39364671	3C 286	J1354–0206
20	NGC 5899	C	2021-03-02	A→D	39375979	3C 286	J1506+4239
		X	2021-03-01	A	39375853	3C 286	J1506+4239
21	NGC 6814	C	2021-03-04	A→D	39380472	3C 286	J1939–1002
		X	2021-03-04	A→D	39376467	3C 286	J1939–1002
22	NGC 7314	C	2021-02-27	A	39338173	3C 48	4.495 Jy	1.8%	J2258–2758
		X	2021-02-28	A	39339300	3C 48	2.697 Jy	0.6%	J2258–2758
23	NGC 7378	C	2021-03-02	A→D	39341061	3C 48	4.491 Jy	1.7%	J2246–1206
		X	2021-02-28	A	39341696	3C 48	2.697 Jy	0.6%	J2246–1206
24	NGC 7465	C	2021-03-02	A→D	39337668	3C 147	J2253+1608
		X	2021-02-28	A	39337786	3C 147	J2253+1608
25	NGC 7479	C	2021-02-28	A	39340326	3C 48	4.494 Jy	1.7%	J2253+1608
		X	2021-02-26	A	39340840	3C 147	J2253+1608

NOTE—**Column 1.** target name. **Column 2.** frequency band observed. **Column 3.** date of observation. **Column 4.** VLA configuration during observation. **Column 5.** NRAO scheduling block ID. **Column 6.** primary calibrator. **Column 7.** interpolated flux density for flaring calibrator at date of observation that primary calibrator was scaled to. **Column 8.** percent difference of flux density from Perley & Butler (2017) as determined by `getcalmodvla`. **Column 9.** secondary phase reference calibrator.

sition). Only a few antennas (2–4) were transitioned per day during the array maneuver, starting with the antennas within the inner core of the array. Our observations concluded on 2021 March 4 and none of outer baselines were affected, maintaining our desired resolution but increasing the largest angular scales to $\sim 240''$ (~ 47 kpc) for the affected data sets. Each target was observed twice, with one observation at C band, from 4 to 8 GHz, and the other at X band, from 8 to 12 GHz. For each scheduling block, observations for absolute flux density scaling and bandpass calibrations were conducted on one of the primary calibrators 3C 48, 3C 138, 3C 147, or 3C 286. A secondary calibrator nearby the target was observed by alternating 2-minute observations for phase referencing with 8-minute observations of the target source. Additionally, calibrator sources were observed for the polarization angle and the polarization crossterms with each scheduling block, but the analysis of polarization properties for each target will be presented in a future publication. Table 2 lists each target’s observation date for each band, the associated scheduling block ID and VLA array configuration, as well as the primary and secondary calibrators used.

We used the Common Astronomy Software Applications (CASA; CASA Team et al. 2022) software package, version 6.6, to calibrate all data. The data reduction was largely done in the same way as in Paper I, with a caveat on the primary calibrator source used for flux density scaling. We first used a priori measurements to determine an initial delay calibration per antenna relative to a reference antenna. We set the flux density of the primary calibrator with `setjy` for observations with 3C 147 and 3C 286 using the Perley-Butler 2017 models (Perley & Butler 2017). However, for the duration of our project, 3C 48 and 3C 138 were both in a flaring state. According to private communications with National Radio Astronomy Observatory (NRAO), the sources are brighter than the Perley-Butler 2017 models, but the flaring is not occurring on a rapid timescale. NRAO conducts monthly monitoring observations of the calibrator sources across all frequency bands and they provided a function which interpolates the flux density for the calibrators at a given date. The function downloads a list of flux density components which are then Fourier transformed with `ft` to model the calibrators across each band. Table 2 lists the interpolated flux densities at 6 GHz and 10 GHz and their percentage differences from the Perley-Butler 2017 models.³ Once the

³ We also checked for flux density differences in 3C 147 but this source showed a 0% difference from the Perley-Butler 2017 model for both bands.

model was set, each observation was calibrated for the bandpass and the complex gain. The calibrated data were inspected for radio frequency interference (RFI), which was then subsequently removed before recalibrating without the RFI affected channels. Once the data were calibrated, the target sources were separated from the measurement sets using `split` and `statwt` was run to reweight the data based on its variance.

2.3. Image Processing

In Figures 1 and 2, we show the multiterm, multiscale, multifrequency synthesis imaging results (MTMFS; Rau & Cornwell 2011, also see Paper I) spanning all calibrated data per band centered at 6 GHz and 10 GHz. For a majority of the images, we used two Taylor terms, multiple scales set to 0, 5, 10, 20, and 40 times the restoring beam, and Briggs deconvolution with a robust weighting of 0. Due to its complex structure, we imaged NGC 1068 with four Taylor terms for both bands to increase the achievable dynamic range.

We iteratively conducted self-calibration on any targets that initially showed imaging artifacts indicative of the instrumental response for the VLA. For each iteration we lightly cleaned an image to generate an approximate model of the source, then applied phase-only gain corrections with increasingly smaller solution intervals until the phases converged. If there were still artifacts, we then applied amplitude based corrections in the same manner. After self-calibration, NGC 1052, NGC 1068, NGC 3079, and NGC 5506 still showed imaging artifacts due to their higher brightness levels.⁴ These sources are dynamic range-limited due to non-closing baseline-based offsets, which is correctable only with significant observing time of a bright calibrator source (see VLA Scientific Memo #152 by R.C. Walker).⁵

Despite these dynamic range limitations, the artifacts in the images do not affect our science goals for this paper, since we are focused on the bright AGN in the center of each image. In Table 3 we report the restoring beam, the theoretical and measured rms noise values, and whether self-calibration was applied for each image. Note that no C-band observation for NGC 3786

⁴ We attempted to use the wideband AW-projection gridded with conjugate beams and a single W-plane (see Bhatnagar et al. 2013), but we found that these images resulted in a loss of faint emission.

⁵ The dynamic range limit for the VLA is $\sim 10,000$ with standard calibration. The current record holder is by Smirnov (2011) using 3C 147 for a dynamic range of 1.6 million.

Table 3. Sensitivity

	Target	Band	Exposure	Restoring Beam	Position Angle	$\sigma_{\text{theor.}}$	σ_{rms}	Self-Cal.
			(s)	(arcsec \times arcsec)	(degree)	($\mu\text{Jy bm}^{-1}$)	($\mu\text{Jy bm}^{-1}$)	
	(1)	(2)	(3)	(4)	(5)	(6)	(7)	(8)
1	NGC 1052	C	2564	0.53×0.25	-45.1	4.01	30.73	p+a
		X	2564	0.28×0.16	-34.2	3.06	21.41	p+a
2	NGC 1068	C	2860	0.40×0.25	-45.4	3.75	12.76	p+a
		X	2860	0.18×0.18	-35.5	3.06	11.40	p+a
3	NGC 1320	C	2560	0.31×0.24	-29.8	3.80	6.42	...
		X	2564	0.30×0.17	-45.5	3.20	7.92	...
4	NGC 2110	C	2558	0.34×0.27	20.5	4.04	6.80	p+a
		X	2374	0.23×0.17	12.2	3.03	16.52	p+a
5	NGC 2782	C	2382	0.33×0.24	-84.0	3.62	6.25	...
		X	2384	0.25×0.16	72.1	3.16	5.54	...
6	IC 2461	C	2560	0.29×0.23	-83.4	3.56	6.53	...
		X	2560	0.27×0.14	74.5	2.68	5.41	...
7	NGC 2992	C	2860	0.50×0.24	36.7	3.43	5.85	...
		X	2860	0.31×0.19	39.9	2.56	8.58	p
8	NGC 3081	C	2860	0.49×0.23	15.6	3.63	6.83	...
		X	2860	0.30×0.14	9.6	2.91	5.48	...
9	NGC 3089	C	2322	0.54×0.21	-0.8	4.03	6.73	...
		X	2800	0.36×0.13	13.8	2.89	6.03	...
10	NGC 3079	C	2384	0.36×0.25	-84.6	3.68	7.05	p+a
		X	1906	0.33×0.14	-71.1	3.16	8.69	p+a
11	NGC 3227	C	2620	0.30×0.23	-68.3	4.28	6.77	...
		X	2624	0.18×0.16	-33.7	2.78	5.34	p
12	NGC 3786	X	2626	0.19×0.15	88.2	2.96	4.93	...
13	NGC 4151	C	2862	0.24×0.23	34.3	3.42	5.01	p+a
		X	2862	0.19×0.14	-84.9	2.68	5.50	p+a
14	NGC 4180	C	2860	0.28×0.25	36.8	3.43	5.41	...
		X
15	NGC 4235	C	2860	0.27×0.23	-9.7	3.63	5.04	...
		X	2860	0.21×0.16	-58.6	2.77	4.89	p
16	NGC 4388	C	2622	0.32×0.25	-53.4	3.72	5.48	...
		X	2626	0.22×0.16	71.6	2.91	6.05	...
17	NGC 4593	C	2862	0.26×0.21	2.2	3.86	18.66	...
		X	2860	0.31×0.15	41.7	2.79	6.11	...
18	NGC 5290	C	2624	0.25×0.22	-56.2	3.72	6.03	...
		X	2622	0.19×0.15	-83.3	2.69	5.14	...
19	NGC 5506	C	2620	0.50×0.23	-47.2	4.12	7.70	p
		X	2622	0.29×0.16	-44.4	3.50	8.02	p
20	NGC 5899	C	2620	0.28×0.23	86.5	3.87	5.51	...
		X	2620	0.17×0.15	74.2	2.80	4.67	...
21	NGC 6814	C	2624	0.45×0.24	-37.1	3.54	6.25	...
		X	2622	0.35×0.15	-41.2	4.09	16.33	...
22	NGC 7314	C	3042	0.48×0.21	7.8	3.39	5.65	...
		X	3040	0.33×0.13	-14.3	2.50	5.02	...
23	NGC 7378	C	3040	0.33×0.21	-19.5	4.07	6.43	...
		X	3040	0.31×0.15	-36.1	2.73	5.20	...
24	NGC 7465	C	2860	0.32×0.23	78.1	4.27	6.20	...
		X	2860	0.17×0.15	64.4	2.68	4.87	...
25	NGC 7479	C	2858	0.26×0.22	-44.0	3.86	6.51	...
		X	2860	0.20×0.16	66.8	2.66	5.00	...

NOTE—**Column 1.** target name. **Column 2.** frequency band observed. **Column 3.** observing time on target source. **Columns 4 & 5.** restoring beam major axis, minor axis, and position angle for MTMFS images. **Column 6.** theoretical rms noise across band. **Column 7.** rms noise measured from MTFMS imaging results. **Column 8.** self-calibration technique applied (p: phase; a: amplitude).

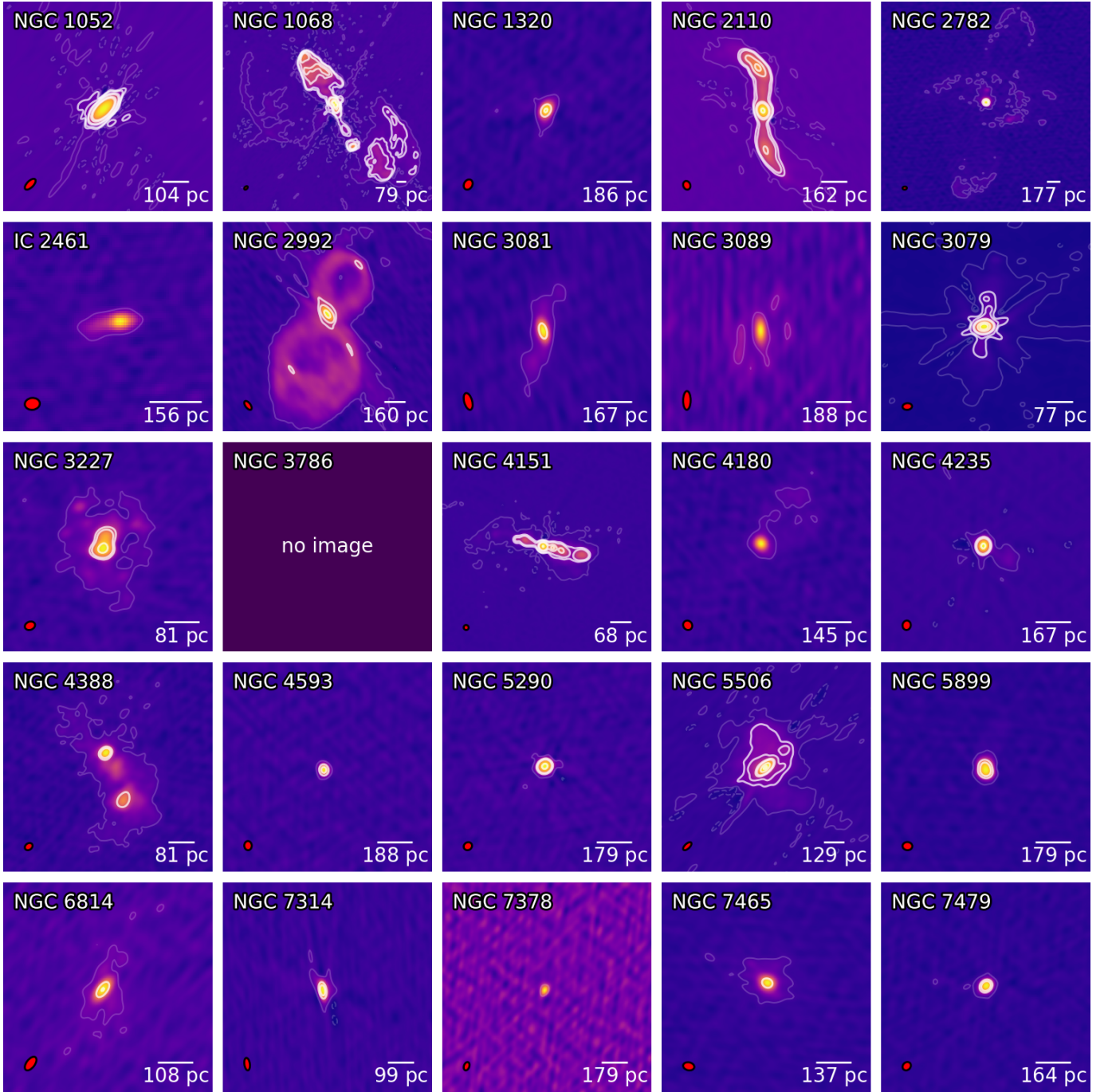


Figure 1. 6 GHz MTMFS imaging results for the VLA FRAMEx sample. The thin contour lines represent $\pm 5 \times \text{rms}$ noise for the respective target (see Table 3). The thick contour lines represent 0.5, 1, 5, 10, 50, and 100 mJy bm^{-1} . The restoring beams are represented by the red ellipse in the bottom left corner. The scale bar represents an angular size of $1''$ and indicates the corresponding length projection.

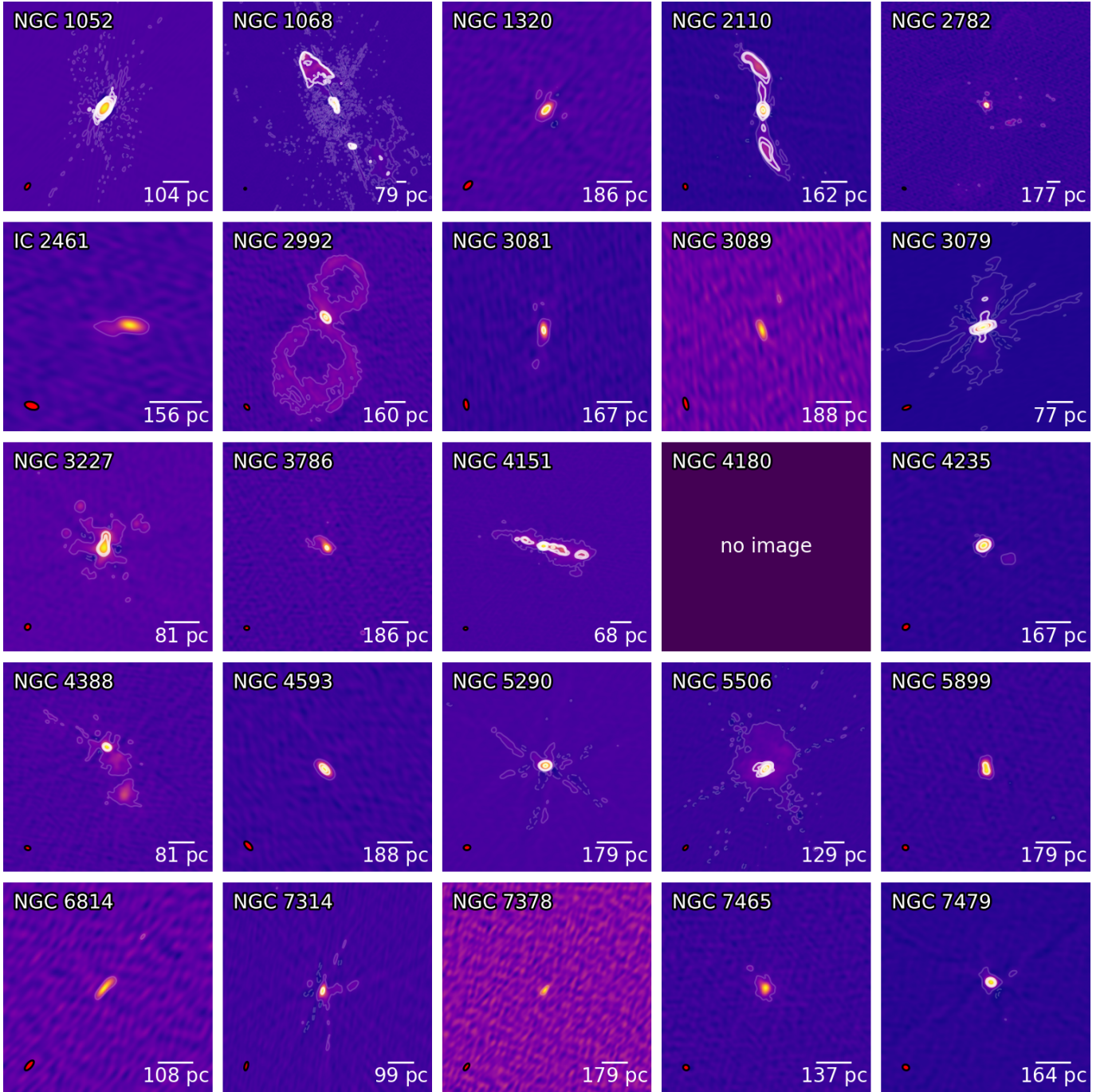


Figure 2. 10 GHz MTMFS imaging results for the VLA FRAMEx sample. The thin contour lines represent $\pm 5 \times \text{rms}$ noise for the respective target (see Table 3). The thick contour lines represent 0.5, 1, 5, 10, 50, and 100 mJy bm^{-1} . The restoring beams are represented by the red ellipse in the bottom left corner. The scale bar represents an angular size of $1''$ and indicates the corresponding length projection.

occurred, and that the X-band observation of NGC 4180 failed due to poor weather.

We used `imfit` on each image with a single 2D Gaussian component to measure the peak flux density of the AGN within a region that was half of the maximum flux density component. We assumed that the AGN was within the point (or nearly point-like) sources detected

in the majority of our imaging results. Similarly for sources with extended features, we assumed the AGN was within the bright point-like object near the pointing center. NGC 1068 contained multiple bright components, and the AGN is south of the brightest peak (Fischer et al. 2023). We did not make a measurement of the nuclear region for this target due to the complex

extended structure blending into the AGN, which prevented a direct measurement of the peak flux density for our imaging results. We report all the peak flux density measurements in Table 4. All uncertainties include the uncertainty on the fit as determined by `imfit`, the rms noise of the cleaned image, and a 5% systematic error (as is typical for the absolute flux calibration of the VLA) added in quadrature.

We also generated image cubes with a typical channel width of 128 MHz. NGC 3089 and NGC 7378 were faint, so we imaged each 2 GHz baseband individually with MTMFS using two Taylor terms. To obtain a consistent flux density measurement for comparison across the channels, we utilized a common (u, v) -taper of $0''.25$ and subsequently convolved each channel to the native beam of the lowest frequency image channel in the C band using `imsmooth`. In the X-band image cubes, we rotated the convolving beam to the position angle of the of the lowest frequency image channel.

2.4. Spectral Energy Distributions

In Figure 3, we present VLA SEDs of the AGNs across 4–12 GHz using peak flux density measurements alongside their respective VLBA measurements from the 6 GHz (deep observation) imaging in FRAMEx III and the multifrequency imaging at 4.4 and 8.6 GHz in FRAMEx V, when available. We used `imfit` to measure the peak flux densities of the AGNs for each image channel using the C-band region we previously defined where the image channel rms noise was used as the uncertainty on the peak flux density. We then used these measurements to fit a spectral index across C band and X band, individually. For several targets we found that there appeared to be a systematic offset at the 8 GHz boundary between C band and X band. Many of the measured offsets between the two bands were within the assumed 5% VLA systematic calibration error, particularly for data calibrated with 3C 286 as the primary flux calibrator. Larger offsets were measured for the brightest source (NGC 1052) and the faintest sources (typically with peak flux densities $\lesssim 2$ mJy/beam). A particularly large offset was measured for NGC 6814, where we measured a 31% offset. It is not entirely clear why the difference between the bands was so large, but both of the C- and X-band observations for this target suffered from significantly more RFI than our other observations. The higher than normal RFI may potentially affect the calibration and compound with the faintness of the source to affect the flux scaling of the source. Thus for the FRAMEx sample we measured the spectral index with curvature across the entire 4–12 GHz

with respect to a reference frequency of 8 GHz while simultaneously fitting for the corrective offset.⁶

In Table 5, we show the spectral index values for C band and X band respectively, as well as the spectral index with curvature across the full frequency range after X-band offset corrections were applied. Note that three targets in our sample were not fit for curvature: NGC 1068 lacked a clear nuclear peak so we did not do any spectral fitting, and both NGC 3089 and NGC 7378 were limited by their faintness and we only measured a spectral index with relatively few data points. The χ^2 value and degrees of freedom for each fit along with the fitted peak flux density at the respective reference frequencies are listed in Appendix A. We found that the data were increasingly underfit as a function of source brightness, and this may be due to some unaccounted for in-band systematic uncertainty.⁷

3. RESULTS

3.1. Brightness Properties

In Figure 4(a) we show the distribution of peak flux densities of the AGNs from Table 4 and we distinguish by whether the target was detected by the VLBA or not. For the VLBA-detected objects, the faintest targets in these VLA observations are NGC 2782, NGC 4388, and NGC 4593, with peak flux densities approximately between 1–3 mJy bm^{-1} . These also happen to be the only three targets that were detected by the 4-hour VLBA deep observations in FRAMEx III, which probed a sensitivity limit of ~ 10 μJy bm^{-1} . The remainder of the VLBA-detected objects all have VLA peak flux densities ranging between 6–170 mJy bm^{-1} except the radio-loud target NGC 1052, which has a peak flux density on the order of 2 Jy bm^{-1} .

For the objects not detected by the VLBA, we note that all have VLA peak flux densities < 8 mJy bm^{-1} . NGC 1320, NGC 3081, NGC 3089, NGC 6814, NGC 7314, and NGC 7465 were observed but not detected in the VLBA deep observations and have VLA peak flux densities ranging between 0.22–1.61 mJy bm^{-1} in the C band and 0.14–0.84 mJy bm^{-1} in the X band. The remaining seven objects (IC 2461, NGC 3227, NGC 3786, NGC 4180, NGC 5899,

⁶ We also attempted fitting with the reference frequency as a free parameter, but this led to poor constraints on the fit parameters.

⁷ Though we did not include this in our final fitting results, we found $\frac{\chi^2}{\text{dof}} \approx 1$ when we included an in-band systematic uncertainty of $0.5\% \times S_{\text{peak}}$ in the error for each image channel.

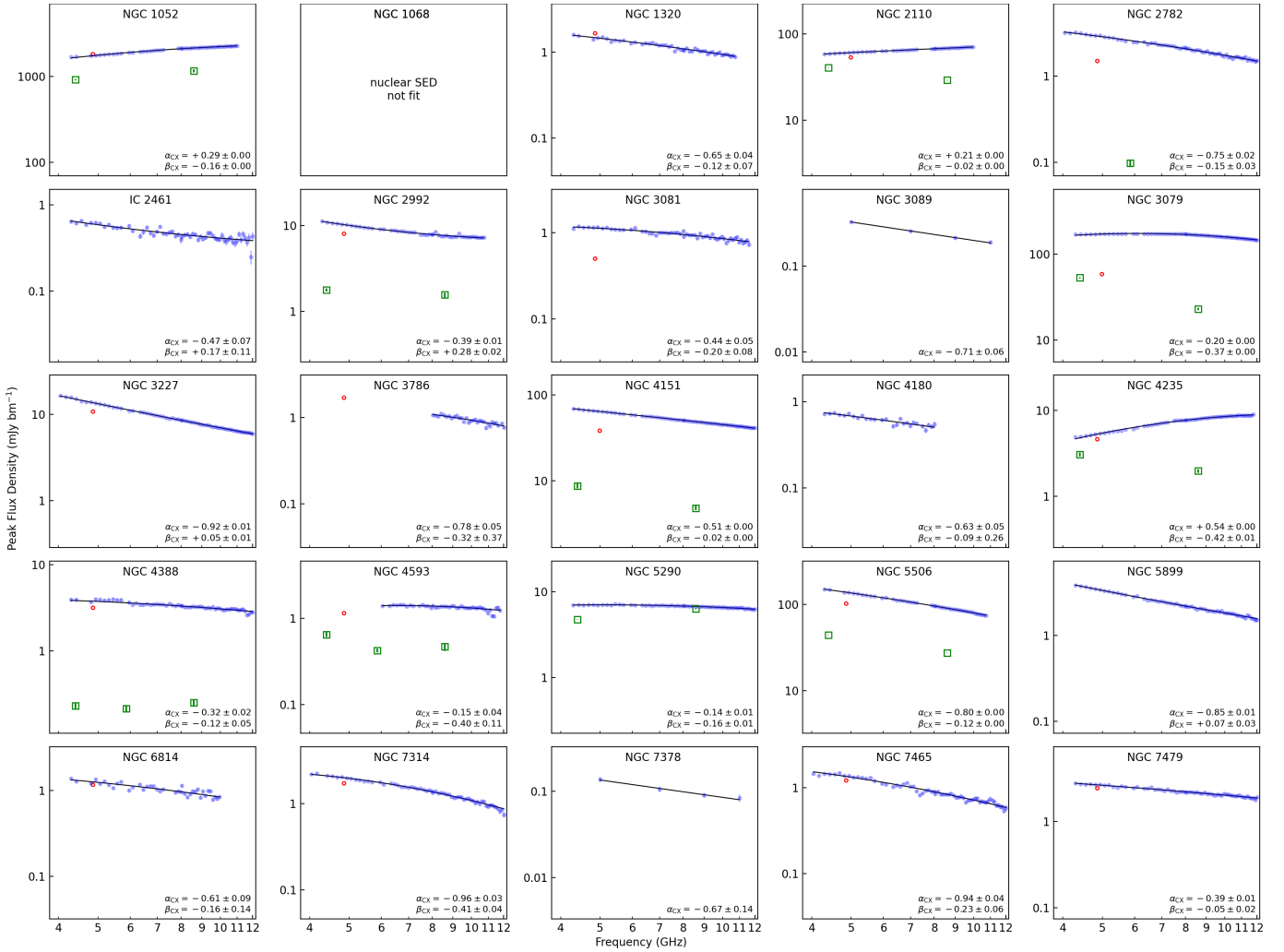


Figure 3. Spectral energy distributions for the VLA FRAMEx sample across 4 – 12 GHz. Each plot spans two orders of magnitude on the vertical axis. The blue circles represent the peak flux density of the AGN from a 2D Gaussian fit on a single channel, where one channel is equal to a single 128 MHz spectral window for all targets except NGC 3089 and NGC 7378 where the channel width is from the 2-GHz baseband. The black line represents the spectral fitting results across 4 – 12 GHz, using a power-law function with spectral curvature and the reference frequency centered at 8 GHz. The red circles represent the archival VLA peak flux densities listed in Table 4 of *FRAMEx I* (4.9 GHz). The green squares represent the peak flux densities for VLBA detected targets from *FRAMEx III* (5.9 GHz) and *FRAMEx V* (4.4 GHz and 8.6 GHz). See *FRAMEx V* for multifrequency VLBA fitting results.

NGC 7378, NGC 7479) have VLA peak flux densities ranging between $0.11 - 7.89 \text{ mJy bm}^{-1}$ in the C band and $0.07 - 3.75 \text{ mJy bm}^{-1}$ in the X band. The deep observation sample was selected from the archival VLA observations with point-like morphology (shown in Figure 3 of *FRAMEx I*) for a higher likelihood of detection with the VLBA. NGC 7479 was not re-observed in *FRAMEx III* and may be a potential candidate for a deep observation, as it has a similar brightness levels to the three detected objects in the deep observations. While NGC 3227 and NGC 5899 appear to have some extended morphology, the peak flux density of the AGNs is also similar to that of the deep observation detec-

tions and may be possible candidates for re-observation. The remaining four objects have VLA peak flux densities $< 1 \text{ mJy bm}^{-1}$ and may be less likely to have detections at VLBA spatial scales.

3.2. Spectral Properties

In Figure 4(b) we show the distribution of spectral index and spectral curvature values from Table 5, and we have again distinguished whether the target was detected in *FRAMEx VLBA* observations or not. When using typical spectral classifications in which $\alpha < -0.5$ is considered steep, $-0.5 \leq \alpha \leq 0.0$ is flat, and $\alpha > 0.0$ is inverted, we observe that there is a clear preference towards a flat or an inverted spectral index for the de-

Table 4. AGN Peak Flux Densities

Target		S_C	S_X
		(mJy bm^{-1})	(mJy bm^{-1})
1	NGC 1052	1881 ± 94	2015 ± 101
2	NGC 1068
3	NGC 1320	1.10 ± 0.06	0.84 ± 0.04
4	NGC 2110	60.1 ± 3.0	68.8 ± 3.4
5	NGC 2782	1.56 ± 0.08	0.80 ± 0.05
6	IC 2461	0.46 ± 0.02	0.32 ± 0.02
7	NGC 2992	60.4 ± 3.02	69.4 ± 3.47
8	NGC 3081	0.85 ± 0.04	0.65 ± 0.03
9	NGC 3089	0.22 ± 0.01	0.14 ± 0.01
10	NGC 3079	167 ± 8	157 ± 8
11	NGC 3227	7.89 ± 0.44	3.75 ± 0.20
12	NGC 3786	...	0.58 ± 0.03
13	NGC 4151	53.4 ± 2.67	39.7 ± 1.99
14	NGC 4180	0.45 ± 0.02	...
15	NGC 4235	6.14 ± 0.31	8.63 ± 0.43
16	NGC 4388	2.79 ± 0.14	2.23 ± 0.11
17	NGC 4593	1.36 ± 0.07	1.27 ± 0.06
18	NGC 5290	6.85 ± 0.34	6.64 ± 0.33
19	NGC 5506	113.0 ± 5.7	74.4 ± 3.7
20	NGC 5899	2.05 ± 0.11	0.86 ± 0.06
21	NGC 6814	1.05 ± 0.05	0.43 ± 0.03
22	NGC 7314	1.61 ± 0.08	0.72 ± 0.04
23	NGC 7378	0.11 ± 0.01	0.07 ± 0.01
24	NGC 7465	0.77 ± 0.04	0.38 ± 0.02
25	NGC 7479	2.35 ± 0.12	2.07 ± 0.10

NOTE—6 GHz and 10 GHz AGN peak flux densities as measured from the MTMFS imaging results shown in Figures 1 and 2. The uncertainties include the 2D Gaussian pixel fitting error, the image rms, and a 5% systematic uncertainty added in quadrature. The highlighted rows indicate VLBA-detected targets.

tected objects. Conversely, we find no inverted indices for the objects not detected by the VLBA, all of those indices are $-1.0 \lesssim \alpha_{CX} \lesssim -0.4$ and they generally tend towards a steep spectral index.

In Table 5, we have indicated nine targets with significant spectral curvature which we also depict in the bottom right of Figure 4(b). We define significant curvature as those meeting the criteria that $\text{abs}(\beta/\sigma_\beta) > 3$ which also reject the null hypothesis that there is no spectral curvature with 99.7% confidence in an F-test. The statistical significance of spectral curvature for each source is depicted in Figure 5, where we show the difference of χ^2 values between the power-law and the power-law with curvature fits as a function of source brightness. There appears to be dependence on the brightness levels for whether significant curvature is de-

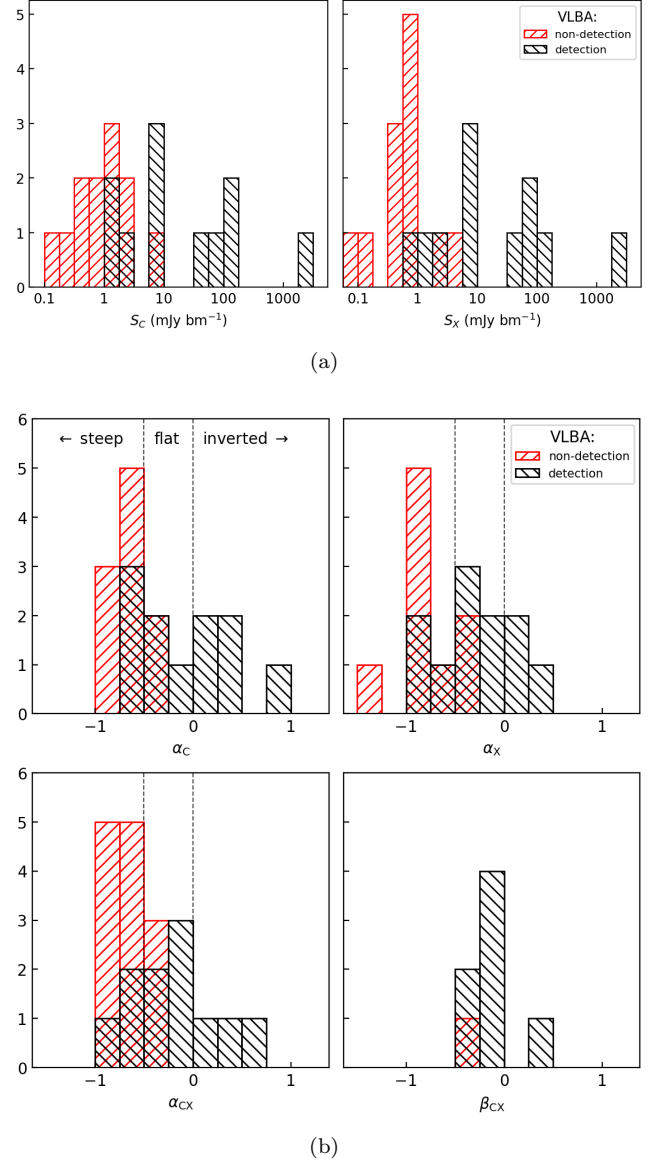


Figure 4. Histograms of: (a) 6 GHz peak flux densities (left) and 10 GHz peak flux densities (right) from Table 4 as measured by the VLA; (b) Corresponding VLA 4 – 8 GHz spectral indices (top left), 8 – 12 GHz spectral indices (top right), 4 – 12 GHz spectral indices (bottom left), and 4 – 12 GHz spectral curvature values with significance (bottom right; see Table 5).

tected since the brightest sources, primarily the VLBA detected objects, indicate significant curvature. VLBA-detected targets with statistically significant curvature are NGC 1052, NGC 2782, NGC 2992, NGC 3079, NGC 4151, NGC 4235, NGC 5290, and NGC 5506. NGC 7314 is the only target with significant curvature that is not detected by the VLBA. NGC 2110, NGC 4388, and NGC 4593 are the three VLBA-detected sources without significant curvature, but detection of

Table 5. AGN Spectral Results

	Target	α_C	α_X	α_{CX}	β_{CX}	Corr.
	(1)	(2)	(3)	(4)	(5)	(6)
1	NGC 1052	$0.39 \pm (<0.01)$	$0.22 \pm (<0.01)$	$0.29 \pm (<0.01)$	$-0.16 \pm (<0.01)$	$+9.2 \pm (<0.1)\%$
2	NGC 1068
3	NGC 1320	-0.58 ± 0.02	-0.66 ± 0.07	-0.65 ± 0.04	-0.12 ± 0.07	$-8.2 \pm 1.7\%$
4	NGC 2110	$0.22 \pm (<0.01)$	$0.24 \pm (<0.01)$	$0.21 \pm (<0.01)$	$-0.02 \pm (<0.01)$	$-0.7 \pm 0.1\%$
5	NGC 2782	-0.64 ± 0.01	-0.83 ± 0.03	-0.75 ± 0.02	-0.15 ± 0.03	$+4.3 \pm 1.0\%$
6	IC 2461	-0.59 ± 0.05	-0.38 ± 0.11	-0.47 ± 0.07	0.17 ± 0.11	$-9.4 \pm 3.3\%$
7	NGC 2992	-0.58 ± 0.01	-0.24 ± 0.02	-0.39 ± 0.01	0.26 ± 0.02	$-5.0 \pm 0.5\%$
8	NGC 3081	-0.32 ± 0.03	-0.54 ± 0.08	-0.45 ± 0.05	-0.20 ± 0.08	$+1.5 \pm 2.1\%$
9	NGC 3089	$-0.71 \pm 0.06^*$
10	NGC 3079	$0.02 \pm (<0.01)$	$-0.38 \pm (<0.01)$	$-0.20 \pm (<0.01)$	$-0.37 \pm (<0.01)$	$-2.5 \pm (<0.1)\%$
11	NGC 3227	$-0.95 \pm (<0.01)$	-0.91 ± 0.01	-0.92 ± 0.01	0.05 ± 0.01	$+2.0 \pm 0.3\%$
12	NGC 3786	...	-0.76 ± 0.04	$-0.78 \pm 0.05^\dagger$	$-0.32 \pm 0.37^\dagger$...
13	NGC 4151	$-0.50 \pm (<0.01)$	$-0.50 \pm (<0.01)$	$-0.51 \pm (<0.01)$	$-0.02 \pm (<0.01)$	$-0.7 \pm (<0.1)\%$
14	NGC 4180	-0.62 ± 0.04	...	$-0.63 \pm 0.05^\ddagger$	$-0.09 \pm 0.26^\ddagger$...
15	NGC 4235	$0.79 \pm (<0.01)$	0.36 ± 0.01	$0.54 \pm (<0.01)$	-0.42 ± 0.01	$-3.5 \pm 0.2\%$
16	NGC 4388	-0.25 ± 0.03	-0.37 ± 0.03	-0.32 ± 0.02	-0.12 ± 0.05	$+2.7 \pm 0.9\%$
17	NGC 4593	-0.08 ± 0.07	-0.28 ± 0.04	-0.15 ± 0.04	-0.40 ± 0.11	$-1.6 \pm 1.3\%$
18	NGC 5290	-0.05 ± 0.01	-0.21 ± 0.01	-0.14 ± 0.01	-0.16 ± 0.01	$-2.5 \pm 0.3\%$
19	NGC 5506	$-0.71 \pm (<0.01)$	$-0.85 \pm (<0.01)$	$-0.80 \pm (<0.01)$	$-0.12 \pm (<0.01)$	$-2.7 \pm (<0.1)\%$
20	NGC 5899	-0.90 ± 0.01	-0.82 ± 0.02	-0.86 ± 0.02	0.07 ± 0.03	$-1.7 \pm 0.7\%$
21	NGC 6814	-0.51 ± 0.03	-0.66 ± 0.19	-0.61 ± 0.09	-0.16 ± 0.14	$+31.0 \pm 2.1\%$
22	NGC 7314	-0.68 ± 0.01	-1.21 ± 0.05	-0.96 ± 0.03	-0.41 ± 0.04	$+13.3 \pm 1.1\%$
23	NGC 7378	$-0.67 \pm 0.14^*$
24	NGC 7465	-0.79 ± 0.02	-0.90 ± 0.06	-0.94 ± 0.04	-0.23 ± 0.06	$-7.0 \pm 1.8\%$
25	NGC 7479	-0.37 ± 0.01	-0.40 ± 0.02	-0.39 ± 0.01	-0.05 ± 0.02	$-10.8 \pm 0.7\%$

NOTE—Spectral fitting results with formal uncertainties for peak flux densities from channelized data for the VLA FRAMEX sample. Highlighted rows indicate VLBA-detected sources. **Column 1.** target name. **Column 2.** 4 – 8 GHz spectral index. **Column 3.** 8 – 12 GHz spectral index **Column 4.** 4 – 12 GHz spectral index at 8 GHz. **Column 5.** 4 – 12 GHz spectral curvature at 8 GHz. Boldface values indicate “significant” curvature, i.e. sources with $\text{abs}(\beta/\sigma_\beta) > 3$ that also pass a nested F-test with 99.7% confidence. **Column 6.** fitted percent shift of X-band data to correct for systematic offset between C band and X band.

*NGC 3089 and NGC 7378 were not fit with curvature due to their faintness.

†NGC 3786 was fit with a reference frequency set to 10 GHz since there were only X-band observations.

‡NGC 4180 was fit with a reference frequency set to 6 GHz since there were only C-band observations.

intrinsic curvature in NGC 4388 and NGC 4593 may be limited in our observations by their faintness. We discuss observational implications of the detection of spectral curvature in the radio in Section 4.2.1.

4. DISCUSSION

4.1. Observational Comparisons

Out of our volume-complete sample of 25 hard X-ray selected AGNs, FRAMEX has thus far detected 12 with the VLBA. In FRAMEX I we suggested that VLA measurements of the emission surrounding the AGNs were likely contaminated by extranuclear host interactions that largely resolve away when observed at the resolution of the VLBA. This is especially true for the sources not detected by the VLBA and the fainter sources de-

tected only by the deep observations in FRAMEX III, where we have recovered only $\sim 4\%$ of the VLA detected emission in NGC 2782 and $\sim 6\%$ in NGC 4388. Two classes of objects emerge from this work when the FRAMEX sources are separated by whether they were detected by the VLBA as depicted in Figure 4. The VLBA detected objects have a clear preference towards the brightest VLA measurements with flat to inverted spectra while the non-detections are the faintest sources and have steep spectra. This could potentially indicate that different radio emission mechanisms are being probed, the measurement of which depending on whether there is a compact radio source.

The non-detected sources with the VLBA have a mean VLA spectral index of $\langle \alpha_{CX}^{ND} \rangle = -0.69$ (with a scatter

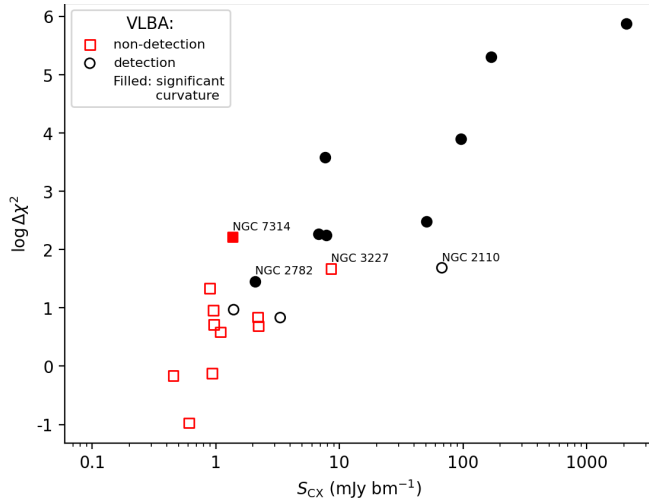


Figure 5. Difference in χ^2 values between power-law model fits with and without spectral curvature, plotted against source brightness at the reference frequency. Black circles represent VLBA-detected objects, while red squares denote non-VLBA-detected objects. Filled markers highlight sources with significant curvature, defined as $\text{abs}(\beta/\sigma_\beta) > 3$ and rejecting the null hypothesis of no curvature at 99.7% confidence.

of $\sigma_{\alpha_{\text{CX}}^{\text{ND}}} = 0.18$), remarkably similar to spectral indices observed in star-forming galaxies (SFGs; see, e.g. Gioia et al. 1982; Condon 1983; Ekers et al. 1989), including the prototypical SFG M82 ($\alpha = -0.8$; Condon 1992). The similarity to that of SFGs could hint that the bulk of the emission observed by the VLA is dominated by recent star-formation activity in H II regions (Condon 1992). However, in Paper I we found that the star formation rate (SFR) from the radio emission surrounding the AGN in NGC 4388 was too luminous for star formation alone when compared to optical tracers, even though the VLBA emission is only $\sim 6\%$ of the VLA emission. That analysis led us to suggest that AGN winds were a plausible source for the excess radio emission in the ISM surrounding the AGN.

Though a full study of SFRs for the FRAMEX sample is beyond the scope of this work, a comparison to hard X-ray selected studies of AGNs may provide some initial clues as to what the origins of radio emission is at VLA resolution. Panessa et al. (2022) observed a hard X-ray selected sample (20 – 40 keV) of 30 AGNs with the VLA to measure matched $\sim 1''$ resolution SEDs at several frequencies between 5 and 45 GHz. Their sample differs from ours by extending to further distances (~ 14 – 1700 Mpc) than the 40 Mpc FRAMEX limit, and it includes some high brightness “radio-loud” AGNs that they define as sources with clear signatures of relativistic jets. The remainder of their targets are considered “radio-quiet” and may be most similar to the FRAMEX

sample, as NGC 1052 is the only object exhibiting a clear jet-like structure (spanning $\sim 27''$, or ~ 2.8 kpc, and terminating in radio lobes in our C-band imaging results). They suggest that the radio quiet AGNs consist of several categories based on their SEDs, with 37% of their sources exhibiting steep spectra from unresolved optically thin synchrotron emission (e.g., from subrelativistic jets, star formation, winds), 10% of their sources having GHz-peaked-spectra (see next section in this work), and the remaining sources having flat spectra compatible with optically thick synchrotron emission (e.g., from a compact jet or magnetically heated corona). Though we do not have as broad of an SED as the Panessa et al. (2022) work, it is possible that our sample may have similar statistics, which may indicate that the flat spectrum VLBA-detected sources in the FRAMEX sample are due to radio emission from an unresolved jet or an optically thick coronal source.

Panessa et al. (2022) go on to suggest following-up with VLBI observations, as the high-resolution observations may help to further constrain the radio emission origins by ruling out processes such as star formation and AGN winds. The FRAMEX project is unique when considering that we now have a uniform set of VLA measurements which are complemented by quasi-simultaneous observations of the same targets with the VLBA and the *Swift* XRT. Our VLA results cross-matched with our VLBA observational detections have clearly distinguished at least two classes of AGN based on their spectra and brightness levels. We will further investigate the consequences of the compact radio source detections (or not) by exploring the potential radio emission mechanisms of our sample in detail in Paper III.

4.2. Spectral Curvature

Spectral curvature can occur at frequencies near the transition between for instance optically thin and optically thick synchrotron emission, but also other emission processes. Detailed spectral curvature measurements in the radio are limited due to bandwidth constraints or the typically static antenna configurations for interferometers, as specified in Section 1. In many cases, spectral curvature is roughly estimated from measurements at three or more frequencies (e.g., Edelson 1987; Chen et al. 2022; Shuvo et al. 2024). Measurements with high frequency resolution have only recently been made possible with the upgraded VLA, which now has a continuous 1 – 50 GHz frequency coverage and can sample a maximum bandwidth of 8 GHz in each polarization. Our VLA spectral measurements were performed for a given spectral range and array configuration and our results motivate gathering even broader spectra with matched

spatial resolutions. However, it may take multiple observing semesters to fully take advantage of the VLA’s antenna configurations in order to gather a matched resolution SED across a broad frequency range, prolonging the scientific analysis. The Next Generation VLA (ngVLA) could provide a solution: by utilizing the sub-arraying capabilities of the observatory, a target could be observed with a compact array at higher frequencies simultaneously with an extended array for the lower frequencies. This would provide the capability to measure an instantaneous full synchrotron spectrum over similar spatial scales, potentially providing evolutionary clues to the origins of the radio source as we discuss in Section 4.2.2.

4.2.1. *Intrinsic Curvature vs. Observational Limitations*

We find that 9 out of the 22 spectral fits show statistically significant curvature in our VLA spectra, and Figure 5 shows that these targets coincide with the brightest sources in the sample. We therefore suggest that radio spectral curvature may be detectable for the fainter sources if there is sufficient signal-to-noise. For our sensitivity limits, the brightness significance threshold appears to be $\sim 5 \text{ mJy bm}^{-1}$, and in Figure 5 we have indicated four sources that straddle this threshold, which we discuss here briefly. NGC 2110 and NGC 3227 are both well above the 5 mJy bm^{-1} brightness threshold but are significantly not curved between 4 – 12 GHz. NGC 3227 is the brightest of the VLBA non-detections and has a similar brightness level to three other targets with a significant curvature. We expect that any intrinsic curvature between 4 – 12 GHz would be apparent, yet this source appears to have a power-law spectrum without any curvature. The lack of VLBA detection for this source combined with having one of the steepest spectral indices of the sample ($\alpha = -0.92 \pm 0.01$) perhaps indicates that radio emission in the target may be dominated by star formation. On the contrary, NGC 2110 is one of the brightest sources in our sample and has an inverted VLA spectrum that appears to be intrinsically not curved at these frequencies, suggesting mechanisms which dominate in the radio over pure star forming processes. Below the 5 mJy bm^{-1} threshold, NGC 7314 is the faintest target with significant spectral curvature and is one of the most curved of our sample at $\beta = -0.41 \pm 0.04$, indicating that strong intrinsic curvature can be apparent in weakly emitting sources. Lastly, NGC 2782 has the lowest significance of the entire sample and is one of the three detected targets in the *FRAMEx III* VLBA deep observations (NGC 4388 and NGC 4593 being the other two), but is the only one with statistically significant curvature.

4.2.2. *Evolutionary Tracks*

The synchrotron spectrum of a statistically representative sample of sources such as *FRAMEx* may be particularly useful in understanding their evolutionary tracks, as was discussed in Section 4.4 of *FRAMEx V*. The multifrequency flux density measurements in *FRAMEx V* suggested a turnover frequency in several sources comparable to that of GHz-peaked spectrum (GPS) sources, which are thought to be compact, young radio sources that peak in flux density $\sim 0.5 - 5 \text{ GHz}$, above which their spectra become steep (Oriente & Dallacasa 2014; O’Dea & Saikia 2021). GPS sources are part of a family of related sources that includes high frequency peakers (HFPs), which peak above 5 GHz, and the compact steep spectrum sources (CSS), which extend from $\sim 1 - 20 \text{ kpc}$ and tend to peak below $\sim 0.5 \text{ GHz}$ (for a recent review see O’Dea & Saikia 2021, and references therein). The peak frequencies in these objects are anti-correlated with the angular size of their host galaxies ($\nu_{\text{pk}} \propto \theta^{-4/5}$) and this may suggest that these objects follow an evolutionary track where the compact and young HFPs evolve into GPS sources, then to CSS objects, and finally into large scale radio galaxies.

Oriente & Dallacasa (2014) measured SEDs for four HFPs with the VLBA and showed that these sources have increasingly resolved morphology, exhibiting single components at low frequencies and resolve into multiple components at higher frequencies. They stacked each sub-component’s respective SEDs at VLBA resolution, and found that the stacked VLBA SEDs characterized the corresponding VLA SEDs quite well: when compared to the previous VLA observations (Dallacasa et al. 2000; Tinti et al. 2005; Oriente et al. 2007), the spectral peaks observed with the VLBA contained $\gtrsim 90\%$ of the corresponding flux density observed by VLA, and only a marginal shift in the peak frequency ($\lesssim 1.5 \text{ GHz}$). This suggests that much of the emission detected at VLBA scales is simply unresolved in the VLA observations for HFPs, indicating a divergence from the *FRAMEx* targets where some sources have emission measured by the VLBA that is $< 10\%$ of the VLA (see Figure 3).

There are also differences in the *FRAMEx* targets when comparing the VLA and VLBA SEDs, in contrast to the previously discussed HFPs. Our VLA results suggest that NGC 1052 clearly peaks above the 12 GHz limiting frequency, but the *FRAMEx V* VLBA results suggest that the nuclear spectrum peaks around $\nu_{\text{pk}} = 5.3 \pm 1.7 \text{ GHz}$. Similarly, NGC 4235 is a VLA source with curvature that peaks at $\nu_{\text{pk}} = 4.3 \pm 1.2 \text{ GHz}$ in the VLBA measurements but the VLA spectrum is inverted at the VLBA peak. Furthermore, NGC 2110

and NGC 4151 have little to no curvature but clearly peak at the VLBA resolution, $\nu_{\text{pk}} = 4.9 \pm 1.7$ GHz and $\nu_{\text{pk}} = 2.9 \pm 1.1$ GHz, respectively. NGC 2992 is another VLBA-detected object with significant VLA curvature (and the only one with positive curvature), but it has a flat spectrum at VLBA resolution. The fact that the VLA spectra differ quite drastically from the VLBA ones may indicate that the FRAMEX sources are not within the same family as GPS, HFPs, and CSS type sources. This may suggest that the emission at VLA resolution when compared to the VLBA emission is indeed extranuclear and we model this excess radio emission in NGC 3079 in the next section.

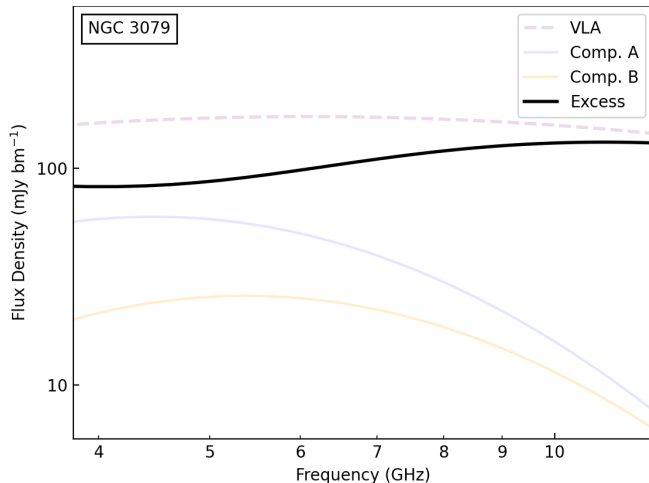


Figure 6. SEDs across 4–12 GHz for emission from various components in NGC 3079. The dashed line represents the fit from the VLA SED from Table 5. The colored solid lines represent the fitted SEDs for the two sub-components from the VLBA measurements in FRAMEX V. The solid black line represents the SED of the excess emission that is detected at VLA resolution but not at VLBA resolution.

4.3. The Substructure of the AGN in NGC 3079

NGC 3079 is one of two targets in the FRAMEX sample that resolves into multiple compact radio components at VLBA resolution FRAMEX IV. This source shows significant curvature at VLA resolution, and there appears to be a spectral break near the 8 GHz frequency edge of the two bands: $\alpha_{\text{C}} = 0.02 \pm 0.01$ and $\alpha_{\text{X}} = -0.38 \pm 0.01$. However, it is not a priori clear whether this is representative of a real spectral break or if it is due to a systematic difference between the two observations for NGC 3079. Given the brightness of NGC 3079, we attempted to calibrate it without phase referencing, to see if there were any effects from bootstrapping the flux densities from the phase calibrator source, but we measured similar indices.

It is highly unlikely that any variability is affecting the measurements, as our two VLA observations for this object occurred consecutively. It is possible however that the measured spectral shape is due to the underlying structure of the sources not resolvable by the VLA. There are two bright radio knots (Components A and B) surrounding the AGN at VLBI resolution (Irwin & Seaquist 1988; Trotter et al. 1998; Sawada-Satoh et al. 2000). Both bright components have been observed to vary, and Component A has continuously increased in brightness since 1992 (see Figure 3 in Fernandez et al. 2023). Component B peaked in brightness around 2005 and has meanwhile steadily decreased in brightness. Additionally, the components are separating, and FRAMEX IV measured a constant projected separation rate of $(0.040 \pm 0.003)c$ for Components A and B since a slowdown event that occurred around 2004.

The two components do appear to have differing spectral peaks at VLBA resolution, and in Figure 6 we show the SED as measured by the VLA in this work compared to the multiwavelength fit from the VLBI measurements in FRAMEX V. Neither component was detected at 22 GHz in FRAMEX V, in contrast to the $\sim 1''$ resolution, 22 GHz VLA observation (C-array configuration), where a peak flux density of $63 \text{ mJy } \text{bm}^{-1}$ is measured (Magno et al. 2025, submitted). This implies that the VLBA spectra of both components peaks in the 4–6 GHz range, perhaps similar to our VLA fitting results. We have therefore modeled the substructure for a third unknown excess emission component that is measured by the VLA but not the VLBA, and we show the resulting model in Figure 6, assuming that the FRAMEX V VLBA spectral structure is representative across the 4–12 GHz band. The modeled radio structure implies that the excess contributor has an approximately flat spectrum, or is slightly increasing with frequency, with a brightness of $\sim 100 \text{ mJy } \text{bm}^{-1}$ (with the flat spectra perhaps continuing to 22 GHz at $1''$ resolution), and is brighter than both Components A and B at high resolution. The faint third component observable by the VLBA is not well constrained and has an insignificant contribution relative to the other components, and cannot account for the excess flux observed by the VLA. The modeled SED implies that in this scenario, the majority of the excess flux in this source must be emitted at distances larger than the resolving capability of the VLBA, i.e., $\gtrsim 1 \text{ pc}$, but smaller than the VLA resolution, i.e., $\lesssim 40 \text{ pc}$, particularly for higher frequencies. The VLBI measurements of NGC 3079 show that there is a complex source encapsulated entirely within the restoring beam of our VLA observations and we will further explore the excess emission in Paper III.

5. SUMMARY AND CONCLUSIONS

We have measured in great detail the circumnuclear radio spectra across 4 – 12 GHz with the VLA for a uniform sample of nearby AGNs, based on a volume-complete hard X-ray selection. The sample has also been observed at milli-arcsecond resolution with the VLBA. Our conclusions are as follows:

1. Our sample distinguishes between two families of AGN emission when analyzing VLA spectra and sorting the results by whether the AGN was detected at VLBA resolution. The VLBA non-detected population have a mean spectral index value of $\langle \alpha_{\text{CX}}^{\text{ND}} \rangle = -0.69$ with a scatter of $\sigma_{\alpha} = 0.18$, in line with optically thin synchrotron spectra, and measures extranuclear radio emission. The VLBA detected population trends toward flat or inverted spectra and measures a combination of extranuclear emission at VLA resolution and nuclear emission at VLBA resolution.
2. We find that the brightest sources have statistically significant spectral curvature, including eight VLBA detected sources and one VLBA non-detected source, implying spectral curvature is detectable with high signal-to-noise. Two sources have no curvature with statistical significance including one VLBA-detected source, NGC 2110.
3. The nonmatching flux densities and shifted spectral peaks at VLA vs VLBA resolution implies that the FRAMEx sample does not appear to have SEDs that correlate well with the spectral signatures observed for GHz peaked spectrum (GPS) sources. The spectral structure from VLA obser-

vations of the GPS objects appears to correlate strongly with their corresponding VLBA observations, further indicating that radio emission for the FRAMEx objects measured by the VLA is indeed extranuclear.

4. We modeled the excess flux density measured by the VLA but not the VLBA for NGC 3079 and found that SED is flat or perhaps slightly inverted. The excess flux density measured by the VLA is on the order of $\sim 100 \text{ mJy beam}^{-1}$ and is produced beyond the approximately parsec spatial scales observed by the VLBA.

Future work in this series will focus on understanding the VLBA vs VLA emission, multiwavelength analysis, and polarization of each source.

ACKNOWLEDGEMENTS

We thank the anonymous referee for the instructive comments. We thank Bryan Butler, Viral Parekh, Rick Perley, Lilia Tremou, and the NRAO Help Desk for their great support in this work.

The National Radio Astronomy Observatory is a facility of the National Science Foundation operated under cooperative agreement by Associated Universities, Inc. The authors acknowledge use of the Very Long Baseline Array under the US Naval Observatory’s time allocation. This work supports USNO’s ongoing research into the celestial reference frame and geodesy.

Facilities: VLA, VLBA

Software: CASA, astropy (Astropy Collaboration et al. 2022), scipy (Virtanen et al. 2020)

REFERENCES

- Astropy Collaboration, Price-Whelan, A. M., Lim, P. L., et al. 2022, *ApJ*, 935, 167, doi: [10.3847/1538-4357/ac7c74](https://doi.org/10.3847/1538-4357/ac7c74)
- Baskin, A., & Laor, A. 2021, *MNRAS*, 508, 680, doi: [10.1093/mnras/stab2555](https://doi.org/10.1093/mnras/stab2555)
- Begelman, M. C., Blandford, R. D., & Rees, M. J. 1984, *Reviews of Modern Physics*, 56, 255, doi: [10.1103/RevModPhys.56.255](https://doi.org/10.1103/RevModPhys.56.255)
- Bhatnagar, S., Rau, U., & Golap, K. 2013, *ApJ*, 770, 91, doi: [10.1088/0004-637X/770/2/91](https://doi.org/10.1088/0004-637X/770/2/91)
- Blandford, R. D., & Königl, A. 1979, *ApJ*, 232, 34, doi: [10.1086/157262](https://doi.org/10.1086/157262)
- CASA Team, Bean, B., Bhatnagar, S., et al. 2022, *PASP*, 134, 114501, doi: [10.1088/1538-3873/ac9642](https://doi.org/10.1088/1538-3873/ac9642)
- Chen, S., Stevens, J. B., Edwards, P. G., et al. 2022, *MNRAS*, 512, 471, doi: [10.1093/mnras/stac530](https://doi.org/10.1093/mnras/stac530)
- Condon, J. J. 1983, *ApJS*, 53, 459, doi: [10.1086/190898](https://doi.org/10.1086/190898)
- . 1992, *ARA&A*, 30, 575, doi: [10.1146/annurev.aa.30.090192.003043](https://doi.org/10.1146/annurev.aa.30.090192.003043)
- Dallacasa, D., Stanghellini, C., Centonza, M., & Fanti, R. 2000, *A&A*, 363, 887, doi: [10.48550/arXiv.astro-ph/0012428](https://doi.org/10.48550/arXiv.astro-ph/0012428)
- de Bruyn, A. G. 1976, *A&A*, 52, 439
- de Bruyn, A. G., & Wilson, A. S. 1978, *A&A*, 64, 433
- Dorland, B., Secrest, N., Johnson, M., et al. 2020, in *Astrometry, Earth Rotation, and Reference Systems in the GAIA era*, ed. C. Bizouard, 165–171, doi: [10.48550/arXiv.2009.02169](https://doi.org/10.48550/arXiv.2009.02169)

- Edelson, R. A. 1987, *ApJ*, 313, 651, doi: [10.1086/165004](https://doi.org/10.1086/165004)
- Ekers, R. D., Wall, J. V., Shaver, P. A., et al. 1989, *MNRAS*, 236, 737, doi: [10.1093/mnras/236.4.737](https://doi.org/10.1093/mnras/236.4.737)
- Fabian, A. C. 2012, *ARA&A*, 50, 455, doi: [10.1146/annurev-astro-081811-125521](https://doi.org/10.1146/annurev-astro-081811-125521)
- Falcke, H., Körding, E., & Markoff, S. 2004, *A&A*, 414, 895, doi: [10.1051/0004-6361:20031683](https://doi.org/10.1051/0004-6361:20031683)
- Fernandez, L. C., Secrest, N. J., Johnson, M. C., & Fischer, T. C. 2023, *ApJ*, 958, 61, doi: [10.3847/1538-4357/acfeda](https://doi.org/10.3847/1538-4357/acfeda)
- Fernandez, L. C., Secrest, N. J., Johnson, M. C., et al. 2022, *ApJ*, 927, 18, doi: [10.3847/1538-4357/ac4b5f](https://doi.org/10.3847/1538-4357/ac4b5f)
- Fischer, T. C., Johnson, M. C., Secrest, N. J., Crenshaw, D. M., & Kraemer, S. B. 2023, *ApJ*, 953, 87, doi: [10.3847/1538-4357/ace1fo](https://doi.org/10.3847/1538-4357/ace1fo)
- Fischer, T. C., Secrest, N. J., Johnson, M. C., et al. 2021, *ApJ*, 906, 88, doi: [10.3847/1538-4357/abca3c](https://doi.org/10.3847/1538-4357/abca3c)
- Gim, H. B., Yun, M. S., Owen, F. N., et al. 2019, *ApJ*, 875, 80, doi: [10.3847/1538-4357/ab1011](https://doi.org/10.3847/1538-4357/ab1011)
- Gioia, I. M., Gregorini, L., & Klein, U. 1982, *A&A*, 116, 164
- Ho, L. C., & Ulvestad, J. S. 2001, *ApJS*, 133, 77, doi: [10.1086/319185](https://doi.org/10.1086/319185)
- Irwin, J. A., & Seaquist, E. R. 1988, *ApJ*, 335, 658, doi: [10.1086/166956](https://doi.org/10.1086/166956)
- Kormendy, J., & Richstone, D. 1995, *ARA&A*, 33, 581, doi: [10.1146/annurev.aa.33.090195.003053](https://doi.org/10.1146/annurev.aa.33.090195.003053)
- Laor, A., Baldi, R. D., & Behar, E. 2019, *MNRAS*, 482, 5513, doi: [10.1093/mnras/sty3098](https://doi.org/10.1093/mnras/sty3098)
- Laor, A., & Behar, E. 2008, *MNRAS*, 390, 847, doi: [10.1111/j.1365-2966.2008.13806.x](https://doi.org/10.1111/j.1365-2966.2008.13806.x)
- Levinson, A., Laor, A., & Vermeulen, R. C. 1995, *ApJ*, 448, 589, doi: [10.1086/175988](https://doi.org/10.1086/175988)
- Lynden-Bell, D. 1969, *Nature*, 223, 690, doi: [10.1038/223690a0](https://doi.org/10.1038/223690a0)
- Merloni, A., Heinz, S., & di Matteo, T. 2003, *MNRAS*, 345, 1057, doi: [10.1046/j.1365-2966.2003.07017.x](https://doi.org/10.1046/j.1365-2966.2003.07017.x)
- O'Dea, C. P., & Saikia, D. J. 2021, *A&A Rv*, 29, 3, doi: [10.1007/s00159-021-00131-w](https://doi.org/10.1007/s00159-021-00131-w)
- Oh, K., Koss, M., Markwardt, C. B., et al. 2018, *ApJS*, 235, 4, doi: [10.3847/1538-4365/aaa7fd](https://doi.org/10.3847/1538-4365/aaa7fd)
- Orienti, M., & Dallacasa, D. 2014, *MNRAS*, 438, 463, doi: [10.1093/mnras/stt2217](https://doi.org/10.1093/mnras/stt2217)
- Orienti, M., Dallacasa, D., & Stanghellini, C. 2007, *A&A*, 475, 813, doi: [10.1051/0004-6361:20078105](https://doi.org/10.1051/0004-6361:20078105)
- Panessa, F., Baldi, R. D., Laor, A., et al. 2019, *Nature Astronomy*, 3, 387, doi: [10.1038/s41550-019-0765-4](https://doi.org/10.1038/s41550-019-0765-4)
- Panessa, F., Chiaraluca, E., Bruni, G., et al. 2022, *MNRAS*, 515, 473, doi: [10.1093/mnras/stac1745](https://doi.org/10.1093/mnras/stac1745)
- Perley, R. A., & Butler, B. J. 2017, *ApJS*, 230, 7, doi: [10.3847/1538-4365/aa6df9](https://doi.org/10.3847/1538-4365/aa6df9)
- Rau, U., & Cornwell, T. J. 2011, *A&A*, 532, A71, doi: [10.1051/0004-6361/201117104](https://doi.org/10.1051/0004-6361/201117104)
- Rush, B., Malkan, M. A., & Edelson, R. A. 1996, *ApJ*, 473, 130, doi: [10.1086/178132](https://doi.org/10.1086/178132)
- Sargent, A. J., Fischer, T. C., Johnson, M. C., et al. 2024, *ApJ*, 961, 230, doi: [10.3847/1538-4357/ad11d4](https://doi.org/10.3847/1538-4357/ad11d4)
- Sawada-Satoh, S., Inoue, M., Shibata, K. M., et al. 2000, *PASJ*, 52, 421, doi: [10.1093/pasj/52.3.421](https://doi.org/10.1093/pasj/52.3.421)
- Shuvo, O. I., Johnson, M. C., Secrest, N. J., et al. 2024, *ApJ*, 961, 109, doi: [10.3847/1538-4357/ad1388](https://doi.org/10.3847/1538-4357/ad1388)
- . 2022, *ApJ*, 936, 76, doi: [10.3847/1538-4357/ac874a](https://doi.org/10.3847/1538-4357/ac874a)
- Smirnov, O. M. 2011, *A&A*, 527, A108, doi: [10.1051/0004-6361/201116435](https://doi.org/10.1051/0004-6361/201116435)
- Tinti, S., Dallacasa, D., de Zotti, G., Celotti, A., & Stanghellini, C. 2005, *A&A*, 432, 31, doi: [10.1051/0004-6361:20041620](https://doi.org/10.1051/0004-6361:20041620)
- Trotter, A. S., Greenhill, L. J., Moran, J. M., et al. 1998, *ApJ*, 495, 740, doi: [10.1086/305335](https://doi.org/10.1086/305335)
- Virtanen, P., Gommers, R., Oliphant, T. E., et al. 2020, *Nature Methods*, 17, 261, doi: [10.1038/s41592-019-0686-2](https://doi.org/10.1038/s41592-019-0686-2)
- Zakamska, N. L., & Greene, J. E. 2014, *MNRAS*, 442, 784, doi: [10.1093/mnras/stu842](https://doi.org/10.1093/mnras/stu842)

APPENDIX

A. ADDITIONAL SED FITTING RESULTS

Table 6 contains both the peak flux densities from the spectral fits at the reference frequencies and the χ^2 values from each fit. For the 4 – 12 GHz fitting results, we conducted an F-test:

$$F(k, N - m - k) = \frac{\Delta\text{RSS}/k}{\text{RSS}_2/(N - m - k)} \quad (\text{A1})$$

where $\Delta\text{RSS} = \text{RSS}_1 - \text{RSS}_2$ is the difference between the residual sums of squares (i.e., the χ^2 values) of the power law model (RSS_1) and the power law with curvature model (RSS_2), N is the number of data points used in the fits, m is the number of parameters in the power law model ($m = 2$), and k is the number of extra parameters in fitting power law with curvature model ($k = 1$).

Table 6. AGN peak flux density and reduced χ^2 from SED fits

Target (1)	Beam (arcsec \times arcsec) (2)	$S_{C,fit}$ (mJy bm^{-1}) (3)	$\frac{\chi^2}{\text{dof}}$ (4)	$S_{X,fit}$ (mJy bm^{-1}) (5)	$\frac{\chi^2}{\text{dof}}$ (6)	$S_{CX,fit}$ (mJy bm^{-1}) (7)	$\frac{\chi^2_{CX}}{\text{dof}}$ (8)	$\frac{\Delta\text{RSS}}{N-m-k}$ (9)	p -value (10)
1	NGC 1052	0.94 \times 0.51	34711/20	1888.84 \pm 0.03	1074/22	2024.91 \pm 0.03	229887/43	751091/43	3.89 \times 10 ⁻¹⁵
2	NGC 1068
3	NGC 1320	0.57 \times 0.50	60/24	1.30 \pm 0.01	31/20	1.09 \pm 0.01	85/45	4/45	1.59 \times 10 ⁻⁰¹
4	NGC 2110	0.63 \times 0.52	648/22	63.32 \pm 0.01	13/14	71.41 \pm 0.03	638/37	49/37	1.01 \times 10 ⁻⁰¹
5	NGC 2782	0.62 \times 0.47	41/28	2.54 \pm 0.01	38/30	1.67 \pm 0.01	86/59	28/59	4.19 \times 10 ⁻⁰⁵
6	IC 2461	0.48 \times 0.44	36/26	0.53 \pm 0.01	43/30	0.45 \pm 0.01	72/57	1/57	4.62 \times 10 ⁻⁰¹
7	NGC 2992	0.86 \times 0.48	111/25	9.05 \pm 0.01	127/20	7.84 \pm 0.02	216/46	176/46	1.92 \times 10 ⁻⁰⁷
8	NGC 3081	0.92 \times 0.45	27/26	1.06 \pm 0.01	29/27	0.95 \pm 0.01	57/54	9/54	5.04 \times 10 ⁻⁰³
9	NGC 3089	0.81 \times 0.40	0.23 \pm (< 0.01)*	0/2
10	NGC 3079	0.72 \times 0.48	56/26	171.07 \pm 0.01	1535/30	161.32 \pm 0.01	21462/57	200477/57	1.11 \times 10 ⁻¹⁶
11	NGC 3227	0.58 \times 0.45	308/28	11.23 \pm 0.01	60/30	6.87 \pm 0.01	343/59	47/59	6.25 \times 10 ⁻⁰³
12	NGC 3786	0.36 \times 0.32	92/29	0.93 \pm 0.01 [†]	91/29	1/29	6.26 \times 10 ⁻⁰¹
13	NGC 4151	0.48 \times 0.46	774/26	58.39 \pm 0.01	341/30	45.45 \pm 0.01	850/57	302/57	3.44 \times 10 ⁻⁰⁵
14	NGC 4180	0.52 \times 0.51	32/25	0.61 \pm 0.01	...	0.61 \pm 0.01 [‡]	32/25	0/25	7.71 \times 10 ⁻⁰¹
15	NGC 4235	0.51 \times 0.48	153/25	6.24 \pm 0.01	308/28	7.65 \pm 0.01	582/54	3819/54	1.11 \times 10 ⁻¹⁶
16	NGC 4388	0.58 \times 0.49	32/25	3.59 \pm 0.02	73/30	3.32 \pm 0.02	109/56	7/56	6.63 \times 10 ⁻⁰²
17	NGC 4593	0.42 \times 0.38	15/12	1.43 \pm 0.02	88/28	1.40 \pm 0.01	95/41	9/41	5.20 \times 10 ⁻⁰²
18	NGC 5290	0.48 \times 0.43	43/26	6.93 \pm 0.01	54/30	6.79 \pm 0.02	80/57	184/57	2.22 \times 10 ⁻¹⁶
19	NGC 5506	0.86 \times 0.46	4333/20	118.81 \pm 0.01	2244/20	95.68 \pm 0.02	7182/41	7883/41	4.26 \times 10 ⁻⁰⁸
20	NGC 5899	0.52 \times 0.45	29/26	2.83 \pm 0.01	63/30	2.19 \pm 0.01	91/57	7/57	4.12 \times 10 ⁻⁰²
21	NGC 6814	0.92 \times 0.47	91/21	1.13 \pm 0.01	44/14	0.96 \pm 0.01	166/36	5/36	2.97 \times 10 ⁻⁰¹
22	NGC 7314	0.89 \times 0.42	27/27	1.72 \pm (< 0.01)	36/30	1.37 \pm 0.01	86/58	164/58	4.00 \times 10 ⁻¹⁵
23	NGC 7378	0.50 \times 0.36	0.10 \pm (< 0.01)*	0/2
24	NGC 7465	0.57 \times 0.45	145/28	1.14 \pm 0.01	42/30	0.89 \pm 0.01	165/59	22/59	7.23 \times 10 ⁻⁰³
25	NGC 7479	0.46 \times 0.45	66/26	2.46 \pm 0.01	66/30	2.21 \pm 0.01	115/57	5/57	1.26 \times 10 ⁻⁰¹

NOTE—Fitting results for peak flux densities from channelized data for the VLA FRAMEx sample. Highlighted rows indicate VLA-detected sources. **Column 1.** target name. **Column 2.** FWHM of restoring beam from matched resolution image cube. **Column 3.** fitted peak flux density at 6 GHz from 4 – 8 GHz power-law fit. **Column 4.** χ^2 from 4 – 8 GHz power-law fit over the degrees of freedom. **Column 5.** fitted peak flux density at 10 GHz from 8 – 12 GHz power-law fit. **Column 6.** χ^2 from 8 – 12 GHz power-law fit over the degrees of freedom. **Column 7.** fitted peak flux density at 8 GHz from 4 – 12 GHz power-law with curvature fit; the 8 – 12 GHz data were corrected by the factor noted in Column 6 of Table 5. **Column 8.** χ^2 from 4 – 12 GHz power-law with curvature fit over the degrees of freedom. **Column 9.** difference of χ^2 values from the power law versus power law with curvature fitting results over the degrees of freedom used in the F-test. **Column 10.** p -value of the F-test. Null hypothesis was rejected in the case of a 99.73% confidence interval.

*NGC 3089 and NGC 7378 were not fit with curvature.

[†]NGC 3786 was fit with a reference frequency set to 10 GHz, so the fitted peak flux density is measured at 10 GHz.

[‡]NGC 4180 was fit with a reference frequency set to 6 GHz, so the fitted peak flux density is measured at 6 GHz.